Emission properties of body-centered cubic elemental metal photocathodes

Tuo Li,[1] Benjamin L. Rickman,[1, a)] and W. Andreas Schroeder[1]

Department of Physics, University of Illinois at Chicago, 845 W. Taylor Street, Chicago, Illinois 60607-7059, USA

(Dated: 10 March 2015)

A first principles analysis of photoemission is developed to explain the lower than expected rms transverse electron momentum measured using the solenoid scan technique for the body-centered cubic Group Vb (V, Nb, and Ta) and Group VIb (Cr, Mo, and W) metallic photocathodes. The density functional theory (DFT) based analysis elucidates the fundamental role that the electronic band structure (and its dispersion) plays in determining the emission properties of solid-state photocathodes and includes evaluation of work function anisotropy using a thin-slab method.

I. INTRODUCTION

Pulsed electron sources generated from laser-driven photoelectron guns are now key components in several of today's research instruments and facilities aimed at improving our understanding of materials, nanoscale systems, and molecular dynamics on fast timescales with high spatial resolution. Ultrafast and femtosecond electron diffraction (UED and FED)[1–7] have provided unprecedented temporal resolution at the atomic scale of laser-driven structural changes (e.g., phase-changes, including melting) of both bulk[3,4,8–13] and nanoscale[14] crystals, and in molecular reaction dynamics[15,16]. Ultrashort (sub-picosecond) x-ray pulses generated using short electron pulses in x-ray free electron lasers (X-FELs), such as at the Linac Coherent Light Source (LCLS), are now able to provide diffractive imaging of atomic structure dynamics[17–21]. The field of time-resolved electron microscopy[22–27], which has imaged reaction front propagation in reactive multilayer foils[28] and the dynamics of phase transitions[20,29,30], crystallization[31–34], and potentially nano-catalysts[35], is now being pushed towards the ultrafast (i.e., sub-nanosecond) regime[25,36–38]. An important experimental attribute of these research instruments is their ability to acquire sufficient data on a *single shot*; as a result, irreversible dynamic processes may be studied with high space-time resolution.

The performance of such cutting-edge research instruments is fundamentally dependent upon the quality of electron pulses produced by their front-end laser-driven electron guns. In particular, the transverse electron beam quality directly determines the fidelity of the measured diffraction pattern in UED, the brightness of X-FEL sources[39–41], and the spatial resolving power in time-resolved electron microscopy if the Rose criterion for adequate image quality ($\sim$100 electrons/pixel on a CCD-based detector[42]) is met. An electron beam with a high transverse brightness[43,44] is characterized by a low rms transverse emittance[45]; a beam parameter that is conserved in propagation through prefect (i.e., non-aberrating) electron optics and is commonly defined as

$\varepsilon_T = \Delta x.\Delta p_T/(m_0 c)$, where Δx is the rms transverse beam size, Δp_T is the rms transverse momentum of the electrons in the pulse, m_0 is the free electron mass, and c is the speed of light in vacuum. If spatial and temporal electron pulse distortion are to be avoided[43,46] when the incident laser pulse duration is less than the time of flight down the gun axis, the short-pulse Child's law[43,47–50] limits the photoemitted electron pulse charge to less than $\varepsilon_0 E_{cath}(\Delta x_{cath})^2$, where E_{cath} is the gun's acceleration field on the photocathode surface, Δx_{cath} is the initial electron beam size, and ε_0 is the vacuum permittivity. As a result, the limiting initial transverse electron pulse brightness is proportional to $E_{cath}/(\Delta p_T)^2$, which favors the use of RF photo-guns due to their higher acceleration fields. The alternative is to significantly reduce the rms transverse momentum, Δp_T, of the electrons generated by the laser-driven photoemission source[51,52].

In this paper, we directly connect the electronic band structure of solid-state photocathodes to the rms transverse momentum of the photoemitted electrons, which thereby provides a means to select (or engineer) high brightness planar photocathode materials. Section II details our experimental solenoid scan[51,53] measurements of Δp_T for polycrystalline body-centered cubic (bcc) Group Vb and VIb elemental metal photocathodes (Cr, Mo, Nb, Ta, V, and W) and shows that the results obtained are inconsistent with prior theoretical formalisms for the rms transverse momentum of the emitted electrons[54,55]. In Section III, we outline a density functional theory (DFT) based analysis of photoemission and show that its results are consistent with the prior analysis of Refs. 54 and 55 for potassium – a close to perfect bcc metal due to its near spherical Fermi surface. Our one-step quantum mechanical[56] DFT-based photoemission analysis is then extended to the Group VIb (Section IV) and Group Vb (Section V) metals and shown to explain the lower values of Δp_T observed in our measurements. The summary discussion of the Paper (Section VI) directly compares the experimental and theoretical values of Δp_T for the six studied bcc metals and contrasts their normalized rms transverse emittance to that measured for Cu photocathodes[52].

―――――――

a)Electronic mail: brickm2@uic.edu
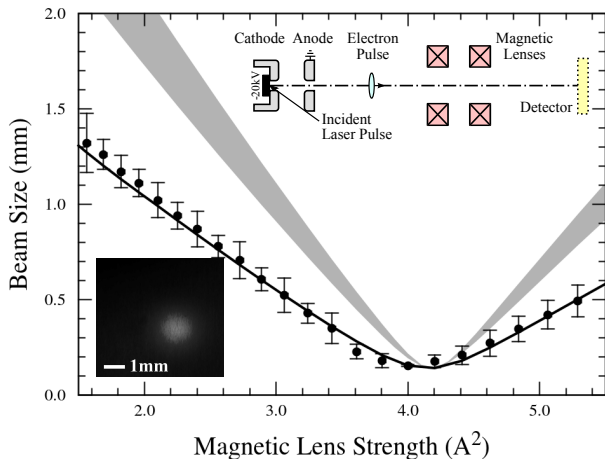
FIG. 1. The measured $HWe^{-1}M$ spot size of the electron beam generated from a polycrystalline Cr photocathode at different lens strengths fitted using our AG model (solid curve). Also shown is the range of theoretical values (shaded region) based on $\Delta p_{T0} = \sqrt{m_0 \Delta E/3}$ [54,55] and $\phi = 4.50(\pm 0.05)\text{eV}$ [61] and an image of the electron beam spot at 1.4A. Inset: Schematic of the experimental geometry for the solenoid scan measurements of Δp_T.

II. EXPERIMENT: SOLENOID SCAN MEASUREMENTS

The experimental method we have employed to determine the rms transverse momentum of electrons emitted from the polycrystalline Group Vb (V, Nb, and Ta) and Group VIb (Cr, Mo, and W) elemental metal photocathodes[51] is the solenoid scan technique[57]. Low charge density electron pulses are produced in a 20kV DC electron gun using ~4ps duration, 261nm ($\hbar\omega = 4.75\text{eV}$) UV laser pulses obtained by harmonic conversion of a diode-pumped, 63MHz repetition rate, femtosecond Yb:KGW laser[58]. As illustrated in the inset of Figure 1, after generation and acceleration in the DC photoelectron gun, the electron pulses are directed to a YAG scintillator screen after passing down the axis of a pair of identical 6.35mm-aperture round magnetic lenses arranged to have counter-propagating coil currents to avoid image rotation effects. Using high-quality 1-to-1 optical imaging, the transverse pulse profile is captured on a CCD camera (5.4μm pixels) as a function of the current in the magnetic lens coils. Knowing the distances between the electron column elements (i.e., the experimental geometry), the fact that a magnetic lens current of 2.03A focuses the electron beam onto the YAG scintillator and that the strength of the magnetic lenses is proportional to the square of the current in their coils[45], allows the measurement technique to be simulated quite accurately using our extension[59] to the analytical Gaussian (AG) electron pulse propagation model[60]. Although our modified AG model now also includes relativistic effects, we note that they do not play an important role in this case as the γ factor is only 1.04 for 20keV electrons.

Figure 1 displays, as an example, the results obtained using the solenoid scan technique for the polycrystalline Cr photocathode. The dependence of the measured electron beam spot size (half-width at $1/e$ maximum ($HWe^{-1}M$)) at the YAG scintillator on the square of the applied magnetic lens current is clearly linear on either side of the beam focus at around 2.03A. The solid line is the extended AG model[59] fit to the data points using just two free parameters: (i) the rms transverse momentum Δp_T of the beam, which determines its convergence (or divergence), and (ii) the focal spot size. The ~50μm "point spread function" of the YAG scintillator plays little role in the AG model simulation as it is significantly smaller than all the measured beam sizes. In this solenoid scan measurement, it is important to ensure (i) that the electron beam propagates down the axis of the magnetic lens system to avoid astigmatism and (ii) that intra-pulse space charge effects are insignificant during electron pulse propagation. The latter condition is well satisfied in our measurements; less than 1000 electrons/pulse are generated from a ~100μm spot size on the photocathode using the ~4ps UV laser pulse, which is two orders of magnitude below the 'short-pulse' Child's Law limit[43,46–50], and AG model simulations indicate that the maximum ~10^4C/m^3 accelerated pulse charge density is also a factor of ~100 below that required to observe space-charge effects in the experiment. As a result, under these conditions, a value for $\Delta p_{T,\text{expt}}$ may be extracted with an accuracy of typically better than 5% using the AG model simulation of the solenoid scan measurement technique (solid line in Figure 1). For the presented case of Cr, we determine that $\Delta p_{T,\text{expt}} = 0.155(\pm 0.005)\sqrt{m_0.\text{eV}}$.

The shaded region plotted in Figure 1 shows the expected range for the variation of the beam size with magnetic lens current for the value of the rms transverse momentum, $\Delta p_{T0} = \sqrt{m_0(\hbar\omega - \phi)/3} = 0.29(\pm 0.03)\sqrt{m_0.\text{eV}}$, predicted by Refs. 54 and 55. Here, we have used a value of $\phi = 4.50\text{eV}$ for polycrystalline Cr[61] with an uncertainty of $\pm 0.05\text{eV}$ and have ignored the Schottky effect (only ~30meV in our case). A similar discrepancy between $\Delta p_{T,\text{expt}}$ and Δp_{T0} has been observed for most of the other polished polycrystalline Group Vb and VIb elemental metal photocathodes; Table I compares our measurements of the rms transverse momentum for all six photocathodes with Δp_{T0} evaluated for $\hbar\omega = 4.75\text{eV}$ using literature values of the work function[61,62]. Only the measurement of $\Delta p_{T,\text{expt}}$ for polycrystalline Mo is in apparent agreement with Δp_{T0}, yet both values are a factor of 1.65 smaller than that observed by Hauri et al.[63] for 6MeV electron pulses, even after accounting for the 0.23eV Schottky effect in their measurement. This discrepancy is likely due to the stronger influence of photocathode surface roughness effects at higher acceleration fields and possibly non-ideal (i.e., non-parabolic) lensing effects in the employed relativistic RF cavity acceleration which would also increase the transverse emittance of the electron pulses. For the Group Vb metals (V, Nb, and Ta), the disparity between

TABLE I. Work functions and rms transverse momentum of polycrystalline bcc metal photocathodes

	ϕ (eV)[a]	$\Delta p_{T,\text{expt}}$ ($\sqrt{m_0 \cdot \text{eV}}$)	Δp_{T0} ($\sqrt{m_0 \cdot \text{eV}}$)
Cr	4.50	0.155±0.005	0.29
Mo	4.60	0.200±0.005	0.22
W	4.55	0.150±0.005	0.26
V	4.30	0.183±0.005	0.39
Nb	4.30	0.185±0.005	0.39
Ta	4.25	0.185±0.005	0.41

[a] References 61 and 62.

$\Delta p_{T,\text{expt}}$ and Δp_{T0} is particularly striking as consistency with Δp_{T0} would require a factor of ~5 reduction in the excess photoemission energy, $\Delta E = \hbar\omega - \phi$. Below, we show that a photoemission analysis using the full electronic band structure of the metal photocathodes provides the explanation for this inconsistency.

III. THEORETICAL PHOTOEMISSION ANALYSIS

Any detailed theoretical analysis of photoemission from a crystalline material requires a knowledge of the band structure near the Fermi level; specifically, the precise energy-momentum relationships, $E(\mathbf{k})$, of the occupied states and their associated local density of states, $g(E, \mathbf{k})$. In addition, knowledge of the photoelectric work function, $\phi_{(ijk)}$, in the (ijk) crystalline direction of photoemission is required in order to determine which occupied states may contribute to the emission and the efficiency of electron photoemission from those states. In sections IV and V below, we present the results of such a photoemission analysis, directed to the evaluation of Δp_T, for the Group VIb (Cr, Mo, and W) and Vb (V, Nb, and Ta) bcc elemental metals. In this section, we introduce our first-principles DFT-based photoemission analysis using the bcc metal potassium (K) as an exemplar. As potassium is a near perfect metal with a close to spherical Fermi surface resulting from a single electron band[64,65], evaluation of its photoemission characteristics provides a canonical test case that can be compared to prior theoretical expressions for the rms transverse momentum[54,55].

The first step in the first-principles photoemission analysis is an evaluation of the electronic band structure of the bcc metals. These calculations within DFT employ the PWscf code of the Quantum-EXPRESSO suite[66] and use ultrasoft pseudopotentials (USPP) within the local density approximation (LDA)[67]. A Monkhorst-Pack[68] set of special k-points and Marzari-Vanderbilt smearing[69] with a broadening of 0.02 Ryd is employed and, for the $4d$, $5d$ and $6p$ metals, relativistic approximations are included[70]. Our calculations of the band structure of K and the Group Vb and VIb metals are in agreement with prior investigations[64,65,71–74], and are
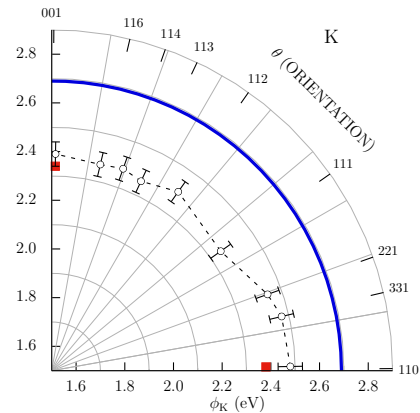

FIG. 2. Polar plot of the photoelectric work function for different crystal faces from the (001) to the (110) face for potassium (K): Theoretical thin-slab DFT-based evaluations (circles); literature values[76] (squares); and a 2.69eV photon energy (solid line).

not changed significantly if we use the generalized gradient approximation (GGA)[75]. The results of these DFT calculations therefore provide accurate four-dimensional momentum-energy ($\mathbf{k}$, E) dispersions and the local density of states $g(E, \mathbf{k})$ for the occupied electronic states below the Fermi level that are involved in photoemission for any particular crystal direction.

In the second step of our photoemission analysis, the photoelectric work function is calculated using the thin-slab method[77] which requires knowledge of the atomic potentials, their lattice positions, and the metal's Fermi level acquired from the bulk DFT band structure evaluations. We employ unrelaxed slabs consisting of 8-12 atomic layers separated by a 15Å vacuum region, which is sufficient to ensure that both the vacuum and average crystal potential reach equilibrium, thus allowing the work function to be determined from the energetic difference between the Fermi and the vacuum levels to an accuracy of typically ±0.05eV. Even if significantly more computationally intensive surface relaxation effects are included, neither the LDA or GGA exchange-correlation potentials appear to offer any less uncertainty than those of experimental values[61,62]. As the arrangement of the atomic potentials in the thin slab depends upon the crystal symmetry and the emission direction perpendicular to the slab (i.e., the crystalline slab orientation), the evaluated work functions ϕ are expected to be dependent upon the (ijk) orientation of the crystal emission face[78] – in agreement with prior studies of bcc metals[62,76,79–83]. As shown in Figure 2 for potassium, this work function anisotropy is not as pronounced as in the Group VIb and Vb metals (see Sections IV and V below), and our evaluations of $\phi_{(ijk)}$ (circles) are in reasonable agreement with experimental data available for the (001) and (110) crystal faces (squares)[76].

Armed with a knowledge of the band structure of the metal photocathode (i.e., $E(\mathbf{k})$ and $g(E, \mathbf{k})$) and the work
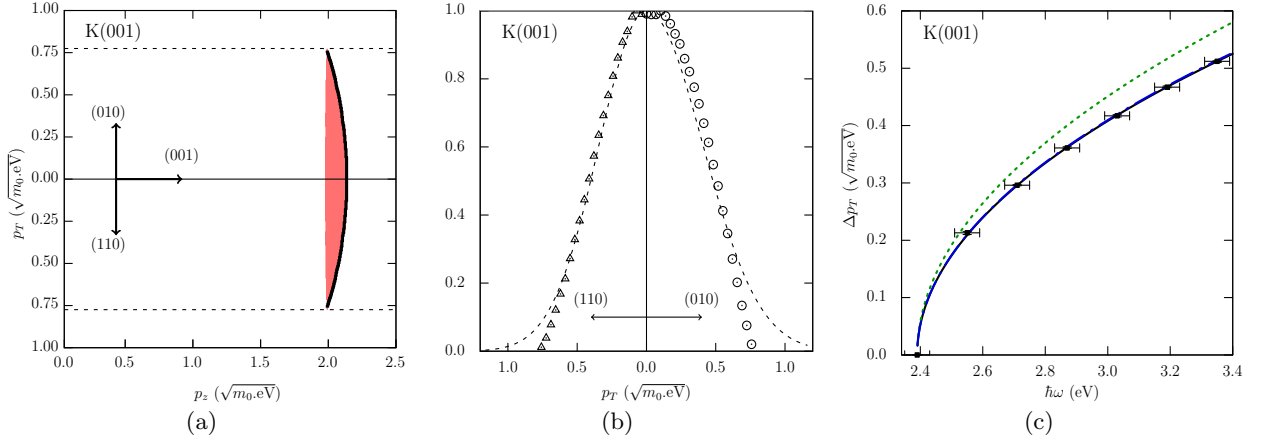
FIG. 3. Results from the DFT-based photoemission analysis for emission from the (001) face of potassium when $\hbar\omega = 2.69$eV: (a) Crystal momentum map of the electronic states (shaded regions) below the Fermi level (solid line) that may photoemit within $p_{T,\text{max.}} = \sqrt{2m_0\Delta E}$ (dashed lines) for the transverse (010) and (110) crystal directions; (b) Transverse momentum distributions of the photoemitted electrons in the (010) and (110) directions (Gaussian fits are guides to the eye); (c) Incident photon energy dependence of the rms transverse momentum Δp_T for electron temperatures $T_e \to 0$ (data points with solid line fit; $\Delta p_T = A\sqrt{m_0\Delta E}$) and $T_e = 300$K (blue dot-dashed line), together with the expected form of $\Delta p_T(\hbar\omega)$ from Refs. 54 and 55 (dashed line).

function anisotropy $\phi_{(ijk)}$, it is straightforward to determine the momentum components of the photoemitted electron and the weighted (by $g(E, \mathbf{k})$) probability of its emission from a particular crystal face over the work function barrier, $T(\mathbf{p}, \mathbf{p}_0)$, where $\mathbf{p}_0 = \hbar\mathbf{k}_0$ is the momentum of the emitted electron in the vacuum. As the momentum of the incident UV photon is negligible in comparison to the momentum of the electron in the crystal ($p = \hbar k >> \hbar\omega/c$) [51], the governing energy-momentum relationship for an instantaneous (one-step) photoemission process[56] involving a virtual optically-excited state may be written as

$$\hbar\omega + E(p_z, p_T) = \phi_{(ijk)} + \frac{1}{2m_0}\left(p_{z0}^2 + p_T^2\right), \quad (1)$$

where the initial electron state energy $E(p_z, p_T)$ is negative below the Fermi level (defined as zero energy). In equation (1), we have written the electron momentum in terms of its longitudinal component $p_z = \hbar k_z$ ($p_{z0} = \hbar k_{z0}$) perpendicular to the (ijk) emission surface in the metal (vacuum), and its transverse component $p_T = \hbar k_T$ parallel to the surface which is conserved during the emission process[84]. The flux transmission probability over the work function barrier is expressed as

$$T(p_z, p_{z0}) = \frac{m_z^*}{m_0}\frac{4p_z p_{z0}}{(p_z + p_{z0})^2}; \quad \frac{1}{m_z^*} = \left|\frac{\partial^2 E}{\partial p_z^2}\right| \quad (2)$$

where the magnitude of the local effective mass in the emission direction, m_z^*, is used to account for both electron-like (positive dispersion) and hole-like (negative dispersion) of the emitting band(s). The close relationship between the band dispersion $E(\hbar\mathbf{k} = \mathbf{p}_z + \mathbf{p}_T)$ below the Fermi level in the photocathode material and the photoemitted electron momentum distribution is clearly evident in equations (1) and (2). In particular, if the band

dispersion restricts electrons with high values of p_T from being emitted (an imaginary p_{z0}), then a reduced value of the emitted rms transverse momentum Δp_T should result.

Figure 3 displays the DFT-based photoemission simulation results for the (001) face of potassium ($\phi_{(001)} = 2.39(\pm 0.05)$eV) when the incident photon energy is 2.69eV (solid line in Figure 2); that is, for an excess energy ΔE of 0.3eV. Figure 3(a) shows the electronic states that contribute to the photoemission (shaded region) below the Fermi level (solid line) along two crystal momentum directions ((010) and (110)) transverse to the (001) emission direction. As expected from the near spherical Fermi surface, the emission states are highly symmetric about the emission direction for this metal. The dashed lines in Figure 3(a) indicate the maximum possible transverse momentum for the photoemitted electrons, which is simply given by $p_{T,\text{max.}} = \sqrt{2m_0\Delta E} \approx 0.77\sqrt{m_0.eV}$. At this value of the transverse momentum, the transmission efficiency over the photoemission barrier, $T(p_z, p_{z0})$, is zero since $p_{z0} = 0$, so that the transverse momentum distributions of the emitted electrons terminate at $p_{T,\text{max.}}$. As the transverse momentum p_T is reduced, more electron states below the Fermi level can contribute to photoemission with those states nearest the Fermi level having the largest local density of states $g(E, \mathbf{k})$ and the highest values of $T(p_z, p_{z0})$. Due to the high symmetry of potassium's band structure, the resulting weighted transverse momentum distributions of the photoemitted electrons are also nearly identical along the (010) and (110) crystal momentum directions (Figure 3(b)). The spatially-averaged value of the rms transverse momentum Δp_T extracted from these p_T distributions for K(001) emission is $0.286\sqrt{m_0.eV}$ – a value which
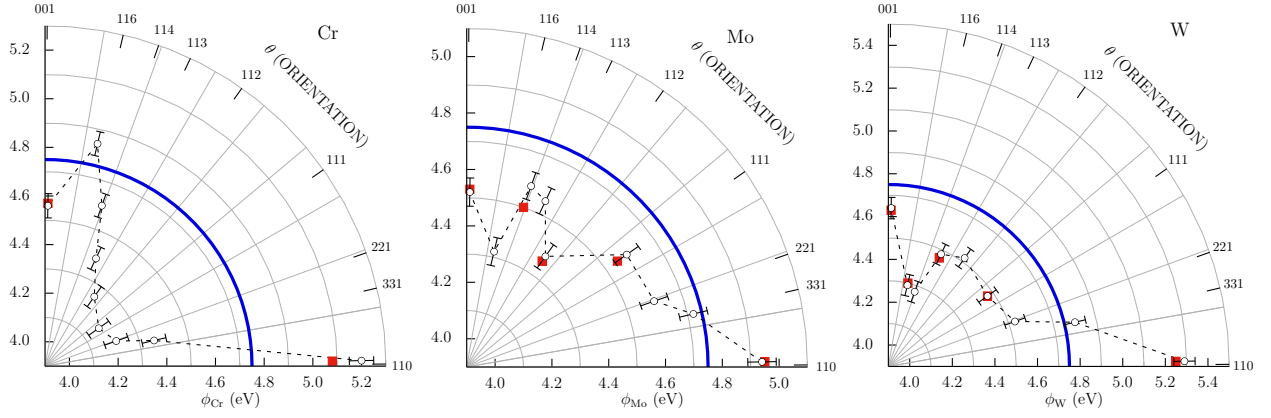
FIG. 4. Polar plot of the photoelectric work function for different crystal faces from the (001) to the (110) face for the Group VIb metals (Cr, Mo, and W): Theoretical thin-slab DFT-based evaluations (circles); literature values for Cr[79,80], Mo[62,85], and W[62,83] (squares); and the experimental 4.75eV UV photon energy (solid line).

is consistent with that predicted by prior analyses[54,55]; $\Delta p_{T0} = \sqrt{m_o \Delta E/3} = 0.316\sqrt{m_0.\text{eV}}$. This agreement is to be expected since the analyses in Refs. 54 and 55 use spherically symmetric bands with an electron mass equal to m_0 and a constant density of states: All are good approximations for potassium as the metal has an effective electron mass at the Fermi level within 20% of m_0 [86], and its Fermi energy of 2.18eV[87] is sufficiently greater than the employed 0.3eV excess photoemission energy which ensures that the approximation of a constant density of states is reasonable.

The dependence of Δp_T on the incident photon energy $\hbar\omega$ determined by the DFT-based photoemission simulation is also in close agreement with the analyses in Refs. 54 and 55. Figure 3(c) shows this dependence using a fit (solid line) to the theoretical data points of the form $\Delta p_T = A\sqrt{m_0(\hbar\omega - \phi_{(001)})}$ together with $\Delta p_{T0} = \sqrt{m_0 \Delta E/3}$ (dashed line)[54,55] for K(001) emission. The extracted value of $A = 0.523$ differs from $1/\sqrt{3}$ by only 10%. Both of these evaluations of the rms transverse momentum are, of course, determined in the zero temperature limit; that is, for an electron temperature $T_e \to 0$ so that no electrons occupy states above the Fermi level. In our DFT-based analysis, this restriction may be lifted by the inclusion of the Fermi-Dirac function $f(E) = 1/(1 + \exp[-(E_F - E)/k_B T_e])$, where k_B is Boltzmann's constant, to describe the occupation of the electronic states around the Fermi energy E_F, albeit for the band structure evaluated for a 'zero temperature' crystal (i.e., where lattice expansion and vibrations are neglected). The blue dot-dashed line in Figure 3(c), just above the solid line, shows the fit to the result of calculating $\Delta p_T(\hbar\omega)$ for the K(001) face with the DFT-based photoemission simulation when $T_e = 300$K (data points not shown). The increase (or change) in Δp_T is only of the order of 1% in this case since E and E_F are both much greater than $k_B T_e$; that is to say, the additional partially populated states above the Fermi level are a small perturbation in the photoemis-

sion simulation. We note that the Boltzmann tail of the Fermi-Dirac distribution will allow photoemission for $\hbar\omega < \phi_{(001)}$ [53], essentially photo-assisted thermionic emission with $\Delta p_T \approx \sqrt{m_0 k_B T_e} = 0.16\sqrt{m_0.\text{eV}}$ for $T_e = 300$K, but this effect is not considered here as the emission efficiency is much reduced. In addition, the DFT-based photoemission analysis as described cannot determine the absolute emission efficiency since the matrix element for photoexcitation into the virtual excited electronic state and electron scattering rates that may limit the lifetime of the emitting state have not been included.

IV. THE GROUP VIb METALS

The Group VIb metals (Cr, Mo, and W) are attractive photocathode materials due to their hardness[88], high melting points[89], and relative chemical inertness (e.g., surface oxidation rate) compared to Cu. Our evaluations of the band structure for these bcc metals, which agree with prior calculations[72,74,90,91], reveal that the Fermi level in these metals crosses several bands. As these bands are also somewhat anisotropic in momentum space, as evidenced by the highly distorted Fermi surface, photoemission will be more complex than for potassium. Fortunately, for all three metals, some experimental data is available for the work function anisotropy $\phi_{(ijk)}$ [62,79,80,83,85] to compare with our thin-slab evaluations.

Figure 4 displays the evaluated work functions (circles) for different crystal faces in the form of a 'polar plot' from (001) to (110), which includes all major orientations expected on the face of a polycrystalline photocathode. Also shown are prior experimental measurements of $\phi_{(ijk)}$ (squares) for Cr[79,80], Mo[62,85], and W[62,83]: Our DFT-based thin-slab evaluations are evidently in good agreement with the literature values within the estimated ± 50meV uncertainty of the theoretical calculations. The data also clearly shows that crystal faces close to the
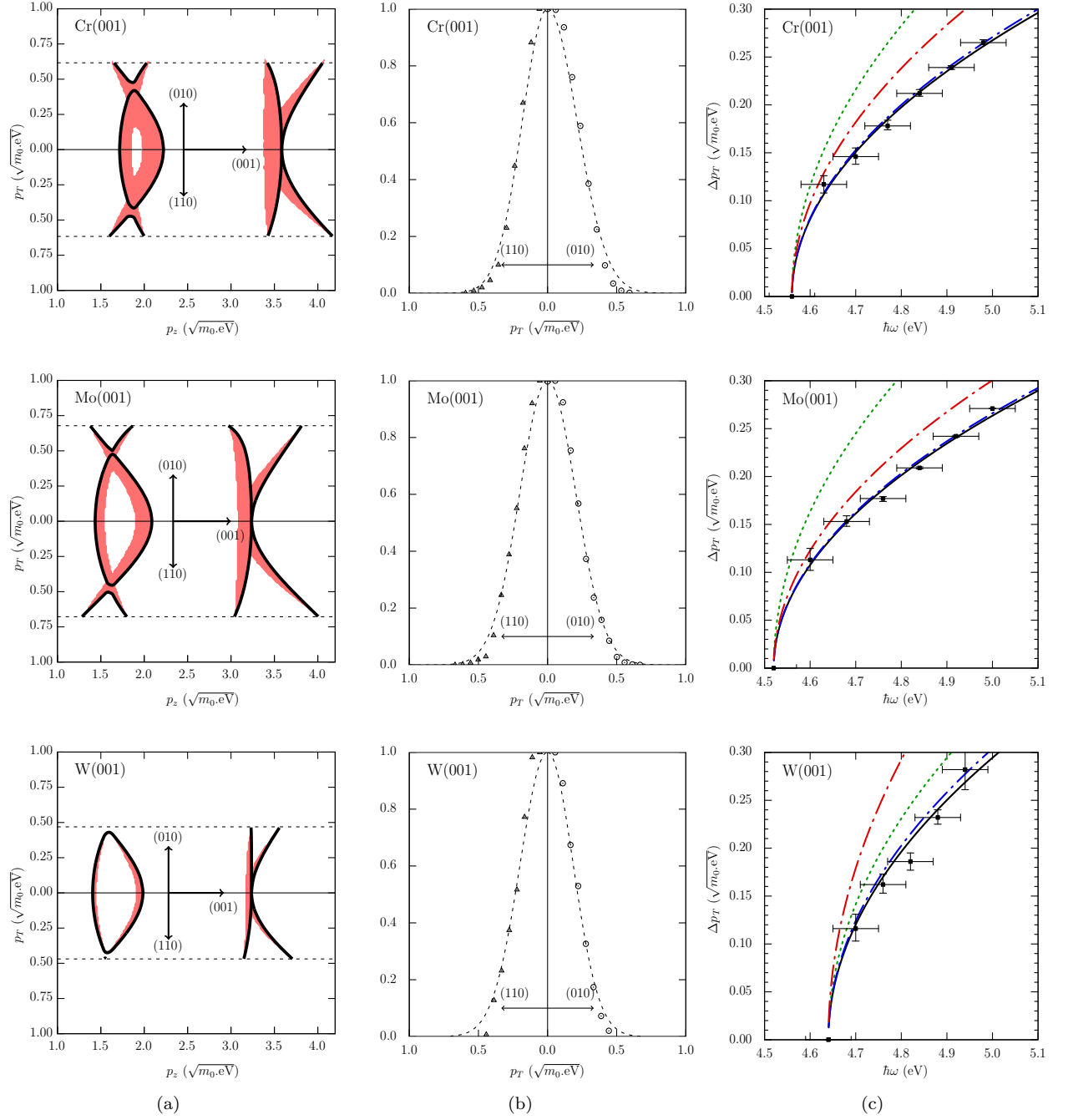
FIG. 5. Results from the DFT-based photoemission analysis for the (001) face of the Group VIb metals (Cr, Mo, and W) for $\hbar\omega$ = 4.75eV. Column (a): Crystal momentum map of the electronic states (shaded regions) below the Fermi level (solid line) that may photoemit within $p_{T,\text{max.}} = \sqrt{2m_0\Delta E}$ (dashed lines) for the transverse (010) and (110) crystal directions. Column (b): Transverse momentum distributions of the photoemitted electrons in the (010) and (110) directions (Gaussian fits are guides to the eye). Column (c): Incident photon energy dependence of the rms transverse momentum Δp_T for electron temperatures $T_e \to 0$ (data points with solid line fit; $\Delta p_T = A\sqrt{m_0\Delta E}$), $T_e = 300K$ and the melting points of each metal (blue and red dot-dashed lines, respectively), together with the expected form of $\Delta p_T(\hbar\omega)$ from Refs. 54 and 55 (dashed line).

(110) orientation of these bcc metals will not emit electrons under our experimental conditions (Section II) as $\phi_{(ijk)}$ is greater than the employed 4.75eV UV laser photon energy (indicated by the solid line). Nonetheless, for the polycrystalline photocathodes used in our measure-ments of Δp_T, the generated electron beam should be intrinsically inhomogeneous with microcrystalline faces closer to the (001) direction dominating the emission. However, for polycrystalline bcc metal surfaces, the (001) crystal face can be expected to be most prevalent[92] and

TABLE II. Photoemission properties of the (001) crystal face of Group VIb metals at $\hbar\omega = 4.75$eV

	$\phi_{(001)}$ (eV)	$\Delta p_{T,\mathrm{DFT}}$ ($\sqrt{m_0\cdot\mathrm{eV}}$)	Δp_{T0} ($\sqrt{m_0\cdot\mathrm{eV}}$)
Cr	4.55($\pm$0.05)	0.168($\pm$0.020)	0.26($\pm$0.03)
Mo	4.52($\pm$0.05)	0.177($\pm$0.019)	0.28($\pm$0.03)
W	4.64($\pm$0.05)	0.160($\pm$0.034)	0.19($\pm$0.04)

hence likely dominate the photoemission properties; typically, for a mechanically worked (in our case polished) bcc metal, the (112) face is the next most frequent covering ∼10% of the surface, while the (111) microcrystal faces only cover a few percent[92]. Careful analysis of the band structure of the Group VIb metals further supports the assertion that the (001) crystal face will dominate the photoemission process, since emission from the (111) or (211) crystal face involves only one band (the Δ_2 band) whereas four sets of electronic states from three bands crossing the Fermi level in the (001) direction[72,74,90,91] contribute to photoemission. The following theoretical analysis will therefore be restricted to (001)-face emission.

The results from the DFT-based analysis for photoemission from the (001) faces of Cr, Mo, and W with $\hbar\omega$ = 4.75eV are displayed in Figure 5. For each element, Figure 5(a) shows the electronic states (shaded regions) below the Fermi level (solid line) that may contribute to photoemission as function of the internal crystal momentum in the (001) direction (p_z) and two transverse momentum (p_T) directions along the (010) and (110) crystal directions. Four separate sets of electronic states from the three bands[72,74,90,91] that cross the Fermi level contribute to photoemission from the (001) face for all three metals; the hole-like Δ_2 band (negative dispersion) and electron-like Δ_2 band (positive dispersion) states from the Fermi surface 'lens' at low p_z, and two electron-like states at higher p_z that are degenerate with the Δ_5 band at $p_T = 0$. All three bands are fairly symmetric about the (001) direction, which leads to relatively isotropic transverse momentum distributions (Figure 5(b)), and hence electron beams with uniform intrinsic divergence. The spatially-averaged values of Δp_T extracted from these momentum distributions are listed in Table II together with the values of $\Delta p_{T0} = \sqrt{m_0\Delta E/3}$ [54,55] computed using $\phi_{(001)}$. In all cases, Δp_{T0} is greater than the results of the DFT photoemission simulation ($\Delta p_{T,\mathrm{DFT}}$) which are in better agreement with our experimental measurements of Δp_T for polycrystalline Group VIb photocathodes (Table I). In fact, the 30% reduction in the rms transverse momentum over Δp_{T0} for both Cr(001) and Mo(001) equates to a reduction in the rms solid angle of divergence (and hence transverse brightness enhancement) for an electron beam by a factor of about 2. Comparison with the K(001) calculation (Figure 3), which was consistent with Δp_{T0}, reveals that the reduced rms transverse momentum for Cr, Mo, and W (001)-face emission is due to the Group VIb metals' band

structure; specifically, the involvement of both electron- and hole-like electronic states and the generally stronger band dispersions. The fact that $\Delta p_{T,\mathrm{DFT}}$ is smallest for W(001) emission is related to the restriction placed on $p_{T,\mathrm{max.}} = \sqrt{2m_0(\hbar\omega - \phi_{(001)})}$ (dashed lines in Figure 5(a)) by the higher value of $\phi_{(001)}$ for tungsten. Similarly, the indistinguishable values of $\Delta p_{T,\mathrm{DFT}}$ for Cr(001) and Mo(001) emission is due to their nearly equal work functions.

Figure 5(c) shows the theoretical dependence of Δp_T on the incident photon energy $\hbar\omega$ for $T_e \to 0$ (data points) together with the form predicted by $\Delta p_{T0} = \sqrt{m_0\Delta E/3}$ (dashed line)[54,55]. For all three metals, the theoretical data is a good fit to $\Delta p_T = A\sqrt{m_0(\hbar\omega - \phi_{(001)})}$ (solid line), giving $A_{\mathrm{Cr(001)}} = 0.403$, $A_{\mathrm{Mo(001)}} = 0.380$, and $A_{\mathrm{W(001)}} = 0.491$ – values significantly less than 0.577. Also shown in Figure 5(c) is the fitted form of $\Delta p_T(\hbar\omega)$ when T_e equals 300K and the melting point of each metal[89] (blue and red dot-dashed lines, respectively) evaluated using the Fermi-Dirac function to describe the occupation of the electronic states generated by the zero temperature DFT band structure calculations (data points not shown). As for K(001) emission (Figure 3(c)), the evaluated $\Delta p_T(\hbar\omega)$ at $T_e = 300$K is indistinguishable from that at 0K within the uncertainty of the DFT-based photoemission simulations. The rms transverse momentum of the emitted electrons does increase for electron temperatures at the melting points of the Group VIb metals with, as would be expected; the increase in Δp_T being most dramatic for W which has the lowest excess photoemission energy, $\Delta E = 0.12$eV, and the highest melting point at 3695K ($k_B T_e = 0.31$eV). This increase is, of course, primarily due to the temperature-dependent partial population of states above the Fermi level which leads to significant emission from states with transverse momenta beyond $p_{T,\mathrm{max.}}$.

V. THE GROUP Vb METALS

Although in general somewhat more reactive than the Group VIb metals, the Group Vb metals (V, Nb, and Ta) are also attractive photocathode materials due again to their hardness[88] and high melting points[89]. Moreover, as shown in Table I, they have lower polycrystalline work functions than their Group VIb counterparts, which translates to a higher photoemission quantum efficiency[54,93]; for polycrystalline photocathodes at $\hbar\omega = 4.75$eV, we have observed that the Group Vb metals have an efficiency a factor of ∼2 greater than the Group VIb metals. This is the primary reason for the use of Ta photocathodes in DTEMs[37,94]. It is also noteworthy that, unlike the Group VIb elements, V, Nb, and Ta are all superconducting and so are directly compatible with superconducting RF photo-guns[95,96].

Our band structure calculations for the bcc Group Vb elements are again in good agreement with prior investigations[72,74,97,98] and show that the Fermi level
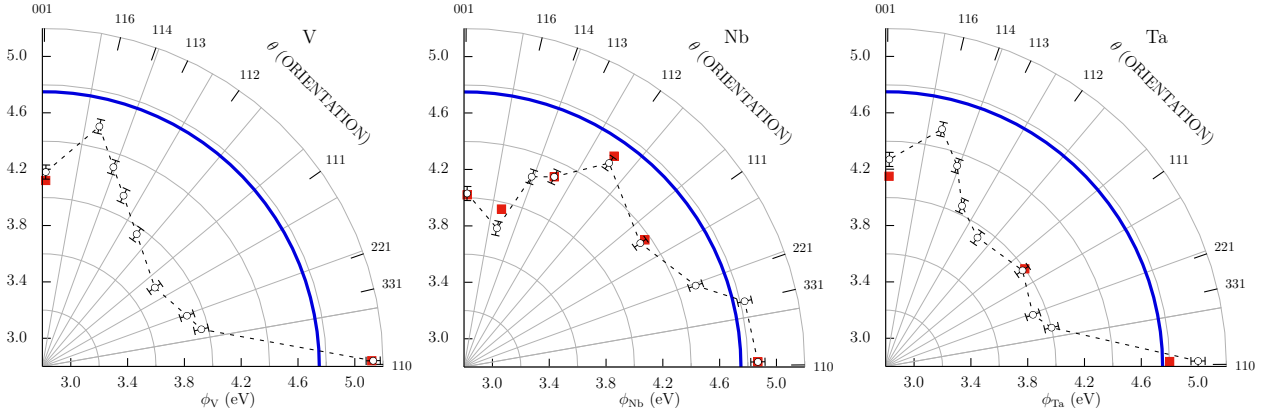
FIG. 6. Polar plot of the photoelectric work function for different crystal faces from the (001) to the (110) face for the Group Vb metals (V, Nb, and Ta): Theoretical thin-slab DFT-based evaluations (circles); literature values for V[76,82], Nb[62,81], and Ta[62] (squares); and the experimental 4.75eV UV photon energy (solid line).

crosses only the Δ_2 band in these metals. This band corresponds to the central 'jack' of the Fermi surface around the Γ-point of the band structure[97–99] and is therefore quite anisotropic. As shown in Figure 6 for different crystal faces from (001) to (110), our evaluations (circles) of the work function anisotropy $\phi_{(ijk)}$ for the Group Vb metals using the thin-slab method[77] are also in reasonable agreement with available data (squares) for V[76,82], Nb[62,81], and Ta[62]. As with the Group VIb elements (Figure 4), $\phi_{(110)}$ is greater than our 4.75eV photon energy (solid line) and their bcc crystal structure means that the (001) microcrystalline face will again likely be the most prevalent[92] and hence dominate the photoemission properties of polycrystalline Group Vb photocathodes.

Figure 7 displays the results from the DFT-based analysis for photoemission from the (001) faces of V, Nb, and Ta when $\hbar\omega = 4.75$eV. The crystal momentum depiction of the electronic states capable of photoemission (shaded regions) below the Fermi level (solid line) in Figure 7(a) for each element clearly shows that emission is only from the hole-like states associated with the 'jack-shaped' Fermi surface centered on the Γ-point of the Brillouin zone. With the exception of Nb at low values of p_z, where band dispersion rather than $p_{T,\text{max.}} = \sqrt{2m_0\Delta E}$ (dashed lines) limits emission in the (110) direction, the emitting states are nonetheless again quite symmetric about the primary (001) crystallographic direction. As a result, the transverse momentum distributions for the emitted electrons from all three Group Vb metals (Figure 7(b)) are again fairly symmetric – the asymmetry in the emission states of Nb not being a strongly contributing factor as electronic states with low values of p_z and high values of p_T have a substantially lower photoemission probability than the other states. This is especially true for photoemission from this hole-like state since, unlike electron-like states with positive dispersion, higher transverse crystal momenta mean lower energy. Indeed, it is clear from the transverse momentum emission distributions in Figure 7(b) that nearly all emitted electrons

TABLE III. Photoemission properties of the (001) crystal face of Group Vb metals at $\hbar\omega = 4.75$eV

	$\phi_{(001)}$ (eV)	$\Delta p_{T,\text{DFT}}$ ($\sqrt{m_0.\text{eV}}$)	Δp_{T0} ($\sqrt{m_0.\text{eV}}$)
V	4.18($\pm$0.05)	0.191($\pm$0.008)	0.44($\pm$0.02)
Nb	4.03($\pm$0.05)	0.204($\pm$0.007)	0.49($\pm$0.02)
Ta	4.27($\pm$0.05)	0.200($\pm$0.010)	0.40($\pm$0.02)

have $p_T < 0.5\sqrt{m_0.\text{eV}}$ for all three Group Vb metals; that is, they are predominantly emitted from the 'jack tip' of the hole-like Δ_2 band. The net result, as shown in Table III, is also a much lower spatially-averaged rms transverse momentum for emission from the (001) face of the Group Vb metals than would be expected from $\Delta p_{T0} = \sqrt{m_0\Delta E/3}$ [54,55] evaluated using the listed values of $\phi_{(001)}$. The extracted values of $\Delta p_{T,\text{DFT}}$ are, however, quite close to our experimental measurements of Δp_T for polycrystalline Group Vb photocathodes (Table I).

Figure 7(c) again shows the theoretical dependence of Δp_T on the incident photon energy $\hbar\omega$ for $T_e \to 0$ (data points) together with the form predicted by $\Delta p_{T0} = \sqrt{m_0\Delta E/3}$ (dashed line)[54,55]. Fitting $\Delta p_T = A\sqrt{m_0(\hbar\omega - \phi_{(001)})}$ to the theoretical data (solid line) gives $A_{\text{V(001)}} = 0.253$, $A_{\text{Nb(001)}} = 0.240$, and $A_{\text{Ta(001)}} = 0.288$ – values less than half of $1/\sqrt{3} \approx 0.577$. This means that the rms solid angle of emission from the (001) crystal face of Group Vb metal photocathodes will be 4-5× less than expected. Moreover, in contrast to their Group VIb counterparts (Figure 5), the values of $\Delta p_T(\hbar\omega)$ evaluated using the DFT-based analysis are only increased by 5-20% as the temperature is increased to the melting point of each metal (red dot-dashed lines in Figure 7(c), data points not shown). This interesting result is again related to the dispersion of the emitting electronic state. For the hole-like emitting state, increasing T_e serves to partially populate states above the Fermi level with gen-
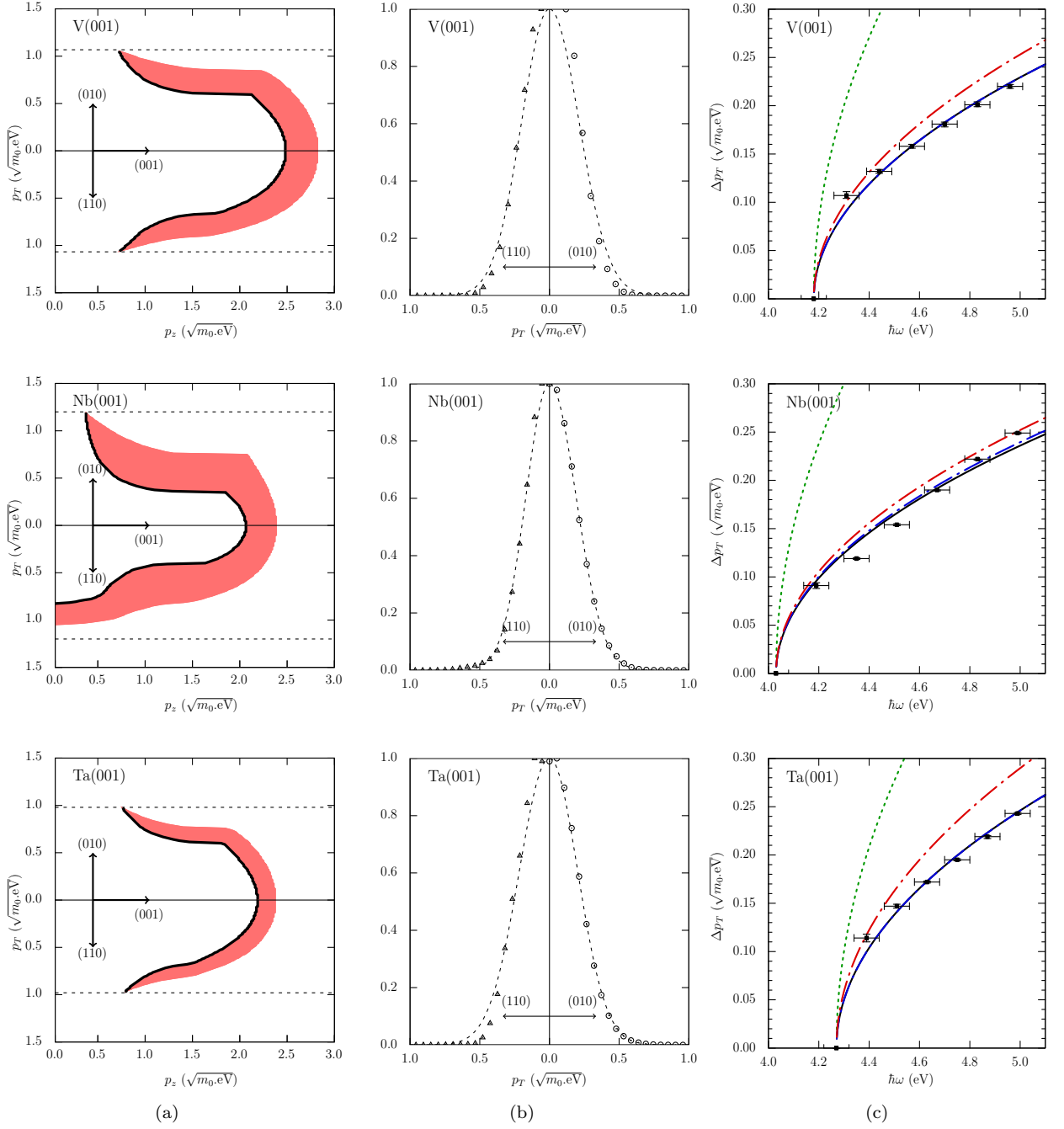
FIG. 7. Results from the DFT-based photoemission analysis for the (001) face of the Group Vb metals (V, Nb, and Ta) for $\hbar\omega$ = 4.75eV. Column (a): Crystal momentum map of the electronic states (shaded regions) below the Fermi level (solid line) that may photoemit within $p_{T,\text{max.}} = \sqrt{2m_0\Delta E}$ (dashed lines) for the transverse (010) and (110) crystal directions. Column (b): Transverse momentum distributions of the photoemitted electrons in the (010) and (110) directions (Gaussian fits are guides to the eye). Column (c): Incident photon energy dependence of the rms transverse momentum Δp_T for electron temperatures $T_e \to 0$ (data points with solid line fit; $\Delta p_T = A\sqrt{m_0\Delta E}$), $T_e = 300$K and the melting points of each metal (blue and red dot-dashed lines, respectively), together with the expected form of $\Delta p_T(\hbar\omega)$ from Refs. 54 and 55 (dashed line).

erally lower values of p_T (Figure 7(a)), thereby leaving Δp_T relatively unchanged. Thus, photoemission from the Group Vb metals is predicted to be significantly less temperature sensitive than from the Group VIb metals.

VI. SUMMARY DISCUSSION

The results obtained using our DFT-based photoemission analysis clearly indicate that a detailed knowledge of the electronic band structure of a photocathode material

is required for a theoretical determination of its electron emission properties. This is fundamentally because the transverse momentum of the electron is conserved in photoemission and it is the band structure in the emission direction which determines the momenta of the states below the Fermi level that may contribute to photoemission under energy conservation. For most photocathode materials, the crystal Fermi surface is quite complex and highly asymmetric (i.e., non-spherical) which can, in principle, result in electron emission with an anisotropic transverse momentum distribution. The transverse momentum distribution of the emitted electrons is also influenced by the local density of states (determined from the band structure calculation) and the transmission probability over the work function barrier. Moreover, this and any other photoemission analysis is further complicated by work function anisotropy, $\phi_{(ijk)}$, which means that a polycrystalline photocathode will, in general, generate an intrinsically inhomogeneous electron beam. We incorporated this complexity into our theoretical analysis by using a thin-slab method to evaluate ϕ for each crystal face using the atomic potentials determined from the DFT band structure calculations.

Our photoemission analysis, which assumes instantaneous one-step emission through a virtual excited state, is successfully benchmarked against prior formalisms[54,55] using potassium – a bcc metal with a near spherical Fermi surface. Extension of our DFT-based analysis to the Group VIb (Cr, Mo, and W) and Group Vb (V, Nb, and Ta) bcc metals has revealed a strong band structure dependence to the rms transverse momentum of the photoemitted electrons. In particular, for photoemission from the (001) crystal face of these metals with 4.75eV photons, the Group Vb elements have significantly lower than expected values of Δp_T due to emission from hole-like electronic states associated with the 'jack-shaped' Fermi surface around the Γ-point of the Brillouin zone. The results obtained for (001)-face emission using the DFT-based analysis are very consistent with our experimental measurements of Δp_T using the solenoid scan technique[51] for polycrystalline Cr, Mo, Nb, Ta, V, and W photocathodes under 261nm UV irradiation. This agreement is shown in Figure 8 where $\Delta p_{T,\text{expt}}$ is plotted against $\Delta p_{T,\text{DFT}}$ for the six bcc Group Vb and VIb metals. The solid line, representing $\Delta p_{T,\text{expt}} = \Delta p_{T,\text{DFT}}$, lies predominantly within the uncertainties of the experimental and theoretical results; the theoretical uncertainty for the Group VIb metals being greater than that for the Group V metals as the ±50meV uncertainty in the value of $\phi_{(001)}$ generates a greater relative uncertainty in $\Delta p_{T,\text{DFT}}$. Although the agreement is also consistent with the assumption that for all six bcc polycrystalline metal photocathodes the (001) microcrystal face is most prevalent[92] and so dominates their photoemission properties, other crystal faces could contribute to the measured $\Delta p_{T,\text{expt}}$. In addition, we note the AG model used to extract $\Delta p_{T,\text{expt}}$ from the solenoid scan measurements is based on a mean field approximation and is known to
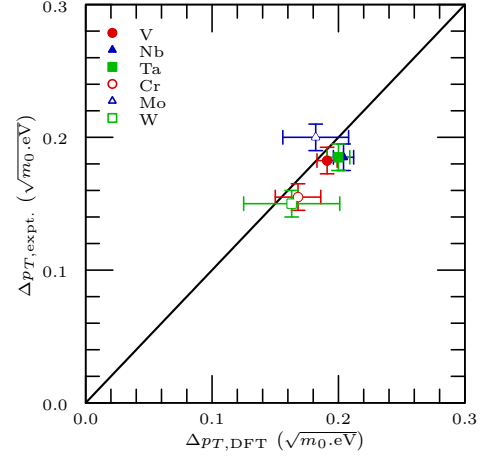

FIG. 8. Comparison of the rms transverse momenta evaluated from the DFT-based photoemission simulation for (001)-face emission, $\Delta p_{T,\text{DFT}}$, with the experimental values obtained for polycrystalline photocathodes from the solenoid scan measurements, $\Delta p_{T,\text{expt}}$, for the six Group Vb (V, Nb, and Ta) and Group VIb (Cr, Mo, and W) metals.

simulate the propagation of real electron pulses with a typical accuracy of a few percent[60].

Future measurements of Δp_T on single-crystal bcc elemental metal photocathodes will be needed to confirm the veracity of the presented DFT-based photoemission analysis. For example, for the studied Group Vb and VIb bcc elemental metals, Δp_T should be measured for the (001), (111), and (110) crystal faces as the first two faces will emit electrons from different regions of the band structure below the Fermi surface and for the latter $\phi > \hbar\omega = 4.75$eV. Measurements of $\Delta p_T(\hbar\omega)$ using a tunable UV radiation source would further examine our theoretical analysis and allow $\phi_{(ijk)}$, a key parameter, to be determined *in situ* for the crystal under study. Nonetheless, our experimental data for all the polycrystalline Group Vb and VIb photocathodes combined with the theoretical trends of the rms transverse momentum with incident photon energy indicate that $\Delta p_{T,\text{expt}} \approx 0.18(\pm 0.04)\sqrt{m_0.\text{eV}}$ for $\hbar\omega = 4.67$eV – the fourth harmonic of a Nd:YAG laser (1064nm) or the third harmonic of a Ti:sapphire laser (ca. 800nm). This value of Δp_T corresponds to a normalized rms transverse emittance $\varepsilon_T/\Delta x = \Delta p_T/(m_0 c) \approx 0.25(\pm 0.05)$ microns/mm, which is less than half of that reported for copper[52,100].

The photoemission analysis has also revealed that the rms transverse momentum of electrons emitted from hole-like (negative dispersion) electronic states is significantly lower than that from electron-like (positive dispersion) states and so the former should be preferred for low divergence (high brightness) photocathode electron sources. Band dispersion provides the explanation for the reduction of Δp_T for hole-like states; unlike for electron-like states, electrons at high p_T in the band structure also have a lower energy and thus a reduced transmission ef-

ficiency over the work function barrier. Hole-like bands also appear to be much less affected by temperature since the majority of partially occupied higher energy bands above the Fermi level that are involved in photoemission will have lower transverse momenta. A comparison of the temperature dependence of Δp_T for (001)-face emission from the Group Vb and VIb metals supports this argument – our DFT-based photoemission analysis indicating that the Δp_T is almost independent of electron temperature T_e for photoemission from the 'jack-shaped' hole-like band in the Group Vb metals. In fact, the value of $\Delta p_T \approx 0.20\sqrt{m_0.\text{eV}}$ determined for these metals at $\hbar\omega = 4.75\text{eV}$ would be equivalent to a strongly temperature invariant mean transverse energy (MTE) of about 40meV. This result could have important practical implications for short-pulse laser-driven photocathodes where laser-induced heating of the electron distribution[53,101] can occur.

VII. ACKNOWLEDGEMENTS

[1] G. Mourou and S. Williamson, Applied Physics Letters **41**, 44 (1982).

[2] R. Srinivasan, V. A. Lobastov, C.-Y. Ruan, and A. H. Zewail, Helvetica Chimica Acta **86**, 1761 (2003).

[3] B. J. Siwick, J. R. Dwyer, R. E. Jordan, and R. J. D. Miller, Science New Series, **302**, 1382 (2003).

[4] J. Cao, Z. Hao, H. Park, C. Tao, D. Kau, and L. Blaszczyk, Applied Physics Letters **83**, 1044 (2003).

[5] G. Sciaini and R. J. D. Miller, Reports on Progress in Physics **74**, 096101 (2011).

[6] C.-Y. Ruan, F. Vigliotti, V. A. Lobastov, S. Chen, and A. H. Zewail, Proceedings of the National Academy of Sciences of the United States of America **101**, 1123 (2004).

[7] J. B. Hastings, F. M. Rudakov, D. H. Dowell, J. F. Schmerge, J. D. Cardoza, J. M. Castro, S. M. Gierman, H. Loos, and P. M. Weber, Applied Physics Letters **89**, 184109 (2006).

[8] S. Williamson, G. Mourou, and J. Li, Physical Review Letters **52**, 2364 (1984).

[9] G. Sciaini, M. Harb, S. G. Kruglik, T. Payer, C. T. Hebeisen, F.-J. M. z. Heringdorf, M. Yamaguchi, M. H.-v. Hoegen, R. Ernstorfer, and R. J. D. Miller, Nature **458**, 56 (2009).

[10] Z. Tao, T.-R. Han, S. Mahanti, P. Duxbury, F. Yuan, C.-Y. Ruan, K. Wang, and J. Wu, Physical Review Letters **109**, 166406 (2012).

[11] B. J. Siwick, J. R. Dwyer, R. E. Jordan, and R. J. D. Miller, Chemical Physics Ultrafast Science with X-rays and Electrons, **299**, 285 (2004).

[12] A. Hanisch-Blicharski, A. Janzen, B. Krenzer, S. Wall, F. Klasing, A. Kalus, T. Frigge, M. Kammler, and M. Horn-von Hoegen, Ultramicroscopy Frontiers of Electron Microscopy in Materials Science, **127**, 2 (2013).

[13] M. Harb, R. Ernstorfer, C. Hebeisen, G. Sciaini, W. Peng, T. Dartigalongue, M. Eriksson, M. Lagally, S. Kruglik, and R. Miller, Physical Review Letters **100**, 155504 (2008).

[14] R. Raman, R. Murdick, R. Worhatch, Y. Murooka, S. Mahanti, T.-R. Han, and C.-Y. Ruan, Physical Review Letters **104**, 123401 (2010).

[15] J. C. Williamson, J. Cao, H. Ihee, H. Frey, and A. H. Zewail, Nature **386**, 159 (1997).

[16] R. C. Dudek and P. M. Weber, The Journal of Physical Chemistry A **105**, 4167 (2001).

[17] H. N. Chapman, A. Barty, M. J. Bogan, S. Boutet, M. Frank, S. P. Hau-Riege, S. Marchesini, B. W. Woods, S. Bajt, W. H. Benner, R. A. London, E. Plönjes, M. Kuhlmann, R. Treusch, S. Düsterer, T. Tschentscher, J. R. Schneider, E. Spiller, T. Möller, C. Bostedt, M. Hoener, D. A. Shapiro, K. O. Hodgson, D. van der Spoel, F. Burmeister, M. Bergh, C. Caleman, G. Huldt, M. M. Seibert, F. R. N. C. Maia, R. W. Lee, A. Szöke, N. Timneanu, and J. Hajdu, Nature Physics **2**, 839 (2006).

[18] K. J. Gaffney and H. N. Chapman, Science **316**, 1444 (2007).

[19] J. Kern, R. Alonso-Mori, R. Tran, J. Hattne, R. J. Gildea, N. Echols, C. Glöckner, J. Hellmich, H. Laksmono, R. G. Sierra, B. Lassalle-Kaiser, S. Koroidov, A. Lampe, G. Han, S. Gul, D. DiFiore, D. Milathianaki, A. R. Fry, A. Miahnahri, D. W. Schafer, M. Messerschmidt, M. M. Seibert, J. E. Koglin, D. Sokaras, T.-C. Weng, J. Sellberg, M. J. Latimer, R. W. Grosse-Kunstleve, P. H. Zwart, W. E. White, P. Glatzel, P. D. Adams, M. J. Bogan, G. J. Williams, S. Boutet, J. Messinger, A. Zouni, N. K. Sauter, V. K. Yachandra, U. Bergmann, and J. Yano, Science **340**, 491 (2013).

[20] F. Schotte, M. Lim, T. A. Jackson, A. V. Smirnov, J. Soman, J. S. Olson, G. N. Phillips, M. Wulff, and P. A. Anfinrud, Science **300**, 1944 (2003).

[21] R. Neutze, R. Wouts, D. van der Spoel, E. Weckert, and J. Hajdu, Nature **406**, 752 (2000).

[22] O. Bostanjoglo and W. R. Horinek, Optik **65**, 361 (1983).

[23] V. A. Lobastov, R. Srinivasan, and A. H. Zewail, Proceedings of the National Academy of Sciences of the United States of America **102**, 7069 (2005).

[24] T. LaGrange, M. R. Armstrong, K. Boyden, C. G. Brown, G. H. Campbell, J. D. Colvin, W. J. DeHope, A. M. Frank, D. J. Gibson, F. V. Hartemann, J. S. Kim, W. E. King, B. J. Pyke, B. W. Reed, M. D. Shirk, R. M. Shuttlesworth, B. C. Stuart, B. R. Torralva, and N. D. Browning, Applied Physics Letters **89**, 044105 (2006).

[25] M. Merano, S. Sonderegger, A. Crottini, S. Collin, P. Renucci, E. Pelucchi, A. Malko, M. H. Baier, E. Kapon, B. Deveaud, and J.-D. Ganière, Nature **438**, 479 (2005).

[26] O. Bostanjoglo, R. Elschner, Z. Mao, T. Nink, and M. Weingärtner, Ultramicroscopy **81**, 141 (2000).

[27] O. Bostanjoglo and M. Weingärtner, Review of Scientific Instruments **68**, 2456 (1997).

[28] J. S. Kim, T. LaGrange, B. W. Reed, M. L. Taheri, M. R. Armstrong, W. E. King, N. D. Browning, and G. H. Campbell, Science **321**, 1472 (2008).

[29] O. Bostanjoglo and R. Liedtke, Physica Status Solidi A **60**, 451 (1980).

[30] T. LaGrange, G. H. Campbell, J. D. Colvin, B. Reed, and W. E. King, Journal of Materials Science **41**, 4440 (2006).

[31] O. Bostanjoglo and G. Schlotzhauer, Physica Status Solidi A **68**, 555 (1981).

[32] O. Bostanjoglo and G. Hoffmann, Physica Status Solidi A **73**, 95 (1982).

[33] M. K. Santala, B. W. Reed, S. Raoux, T. Topuria, T. LaGrange, and G. H. Campbell, Physica Status Solidi B **249**, 1907 (2012).

[34] M. K. Santala, B. W. Reed, S. Raoux, T. Topuria, T. LaGrange, and G. H. Campbell, Applied Physics Letters **102**, 174105 (2013).

[35] D. J. Masiel, B. W. Reed, T. B. LaGrange, G. H. Campbell, T. Guo, and N. D. Browning, Chemical Physics Physical Chemistry **11**, 2088 (2010).

[36] W. E. King, G. H. Campbell, A. Frank, B. Reed, J. F. Schmerge, B. J. Siwick, B. C. Stuart, and P. M. Weber, Journal of Applied Physics **97**, 111101 (2005).

[37] M. R. Armstrong, K. Boyden, N. D. Browning, G. H. Campbell, J. D. Colvin, W. J. DeHope, A. M. Frank, D. J. Gibson, F. Hartemann, J. S. Kim, W. E. King, T. B. LaGrange, B. J. Pyke, B. W. Reed, R. M. Shuttlesworth, B. C. Stuart, and B. R. Torralva, Ultramicroscopy **107**, 356 (2007).

[38] M. R. Armstrong, B. W. Reed, B. R. Torralva, and N. D. Browning, Applied Physics Letters **90**, 114101 (2007).

[39] K.-J. Kim, Y. Shvyd'ko, and S. Reiche, Physical Review Letters **100**, 244802 (2008).

[40] "Compact X-ray Light Source," Workshop PNNL-22145 (Pacific Northwest National Laboratory, Richland, Washington, 2012).

[41] Z. Huang and K.-J. Kim, Physical Review Special Topics - Accelerators and Beams **10**, 034801 (2007).

[42] A. Rose, in *Advances in Electronics and Electron Physics*, Vol. 1, edited by L. Marton (Academic Press, 1948) pp. 131–166.

[43] I. Bazarov, B. Dunham, and C. Sinclair, Physical Review Letters **102**, 104801 (2009).

[44] M. J. Rhee, Physics of Fluids B: Plasma Physics (1989-1993) **4**, 1674 (1992).

[45] M. Reiser, *Theory and Design of Charged Particle Beams* (Wiley, New York, 2008).

[46] Á. Valfells, D. W. Feldman, M. Virgo, P. G. O'Shea, and Y. Y. Lau, Phys. Plasmas **9**, 2377 (2002).

[47] C. Child, Physical Review (Series I) **32**, 492 (1911).

[48] I. Langmuir, Physical Review **21**, 419 (1923).

[49] T. Srinivasan-Rao, J. Fischer, and T. Tsang, Journal of Applied Physics **69**, 3291 (1991).

[50] T. Anderson, I. V. Tomov, and P. M. Rentzepis, Journal of Applied Physics **71**, 5161 (1992).

[51] B. L. Rickman, J. A. Berger, A. W. Nicholls, and W. A. Schroeder, Physical Review Letters **111**, 237401 (2013); *ibid.* **113**, 239904 (2014), (Erratum).

[52] D. Dowell, I. Bazarov, B. Dunham, K. Harkay, C. Hernandez-Garcia, R. Legg, H. Padmore, T. Rao, J. Smedley, and W. Wan, Nucl. Instrum. Methods A **622**, 685 (2010).

[53] J. A. Berger, B. L. Rickman, T. Li, A. W. Nicholls, and W. Andreas Schroeder, Appl. Phys. Lett. **101**, 194103 (2012).

[54] D. Dowell and J. Schmerge, Physical Review Special Topics - Accelerators and Beams **12**, 074201 (2009).

[55] K. L. Jensen, P. G. O'Shea, D. W. Feldman, and J. L. Shaw, Journal of Applied Physics **107**, 014903 (2010).

[56] G. D. Mahan, Physical Review B **2**, 4334 (1970).

[57] W. Graves, L. DiMauro, R. Heese, E. Johnson, J. Rose, J. Rudati, T. Shaftan, and B. Sheehy, in *Particle Accelerator Conference*, Vol. 3 (2001) pp. 2227–2229; pp. 2230–2232.

[58] J. A. Berger, M. J. Greco, and W. A. Schroeder, Opt. Express **16**, 8629 (2008).

[59] J. A. Berger and W. A. Schroeder, Journal of Applied Physics **108**, 124905 (2010).

[60] A. M. Michalik and J. E. Sipe, J. Appl. Phys. **99**, 054908 (2006).

[61] D. Eastman, Physical Review B **2**, 1 (1970).

[62] H. B. Michaelson, Journal of Applied Physics **48**, 4729 (1977).

[63] C. Hauri, R. Ganter, F. Le Pimpec, A. Trisorio, C. Ruchert, and H. Braun, Physical Review Letters **104**, 234802 (2010).

[64] J. Reitz and A. Overhauser, Physical Review **171**, 749 (1968).

[65] F. Ham, Physical Review **128**, 2524 (1962).

[66] P. Giannozzi, S. Baroni, N. Bonini, M. Calandra, R. Car, C. Cavazzoni, D. Ceresoli, G. L. Chiarotti, M. Cococcioni, I. Dabo, A. D. Corso, S. d. Gironcoli, S. Fabris, G. Fratesi, R. Gebauer, U. Gerstmann, C. Gougoussis, A. Kokalj, M. Lazzeri, L. Martin-Samos, N. Marzari, F. Mauri, R. Mazzarello, S. Paolini, A. Pasquarello, L. Paulatto, C. Sbraccia, S. Scandolo, G. Sclauzero, A. P. Seitsonen, A. Smogunov, P. Umari, and R. M. Wentzcovitch, Journal of Physics: Condensed Matter **21**, 395502 (2009).

[67] K. F. Garrity, J. W. Bennett, K. M. Rabe, and D. Vanderbilt, Computational Materials Science **81**, 446 (2014).

[68] H. Monkhorst and J. Pack, Physical Review B **13**, 5188 (1976).

[69] N. Marzari, D. Vanderbilt, A. De Vita, and M. Payne, Physical Review Letters **82**, 3296 (1999).

[70] M. Sigalas, D. Papaconstantopoulos, and N. Bacalis, Physical Review B **45**, 5777 (1992).

[71] M. Halloran, J. Condon, J. Graebner, J. Kunzier, and F. Hsu, Physical Review B **1**, 366 (1970).

[72] L. Mattheiss, Physical Review **139**, A1893 (1965).

[73] R. Parker and M. Halloran, Physical Review B **9**, 4130 (1974).

[74] T. Loucks, Physical Review **139**, A1181 (1965).

[75] J. Perdew, K. Burke, and M. Ernzerhof, Physical Review Letters **77**, 3865 (1996).

[76] H. Skriver and N. Rosengaard, Physical Review B **46**, 7157 (1992).

[77] C. J. Fall, N. Binggeli, and A. Baldereschi, Journal of Physics: Condensed Matter **11**, 2689 (1999).

[78] R. Smoluchowski, Physical Review **60**, 661 (1941).

[79] R. E. Thomas and G. A. Haas, Journal of Applied Physics **43**, 4900 (1972).

[80] C. Fu and A. Freeman, Physical Review B **33**, 1755 (1986).

[81] R. P. Leblanc, B. C. Vanbrugghe, and F. E. Girouard, Canadian Journal of Physics **52**, 1589 (1974).

[82] S. Ohnishi, C. L. Fu, and A. J. Freeman, Journal of Magnetism and Magnetic Materials **50**, 161 (1985).

[83] S. Surma, Physica Status Solidi A **183**, 307 (2001).

[84] F. Himpsel, Advances in Physics **32**, 1 (1983).

[85] D. Jacobson and A. Campbell, Metall. Trans. **2**, 3063 (1971).

[86] A. Piróth and J. Sólyom, *Fundamentals of the Physics of Solids: Volume II: Electronic Properties*, Fundamentals of the Physics of Solids (Springer, 2008).

[87] D. Papaconstantopoulos, *Handbook of the Band Structure of Elemental Solids* (Springer, 2014).

[88] D. Tabor, *The Hardness of Metals*, Vol. 10 (Clarendon Press, 1951).

[89] W. Haynes, ed., *CRC Handbook of Chemistry and Physics*, 95th ed., CRC Handbook of Chemistry and Physics (CRC Press, 2014).

[90] R. Iverson and L. Hodges, Physical Review B **8**, 1429 (1973).

[91] D. Laurent, J. Callaway, J. Fry, and N. Brener, Physical Review B **23**, 4977 (1981).

[92] I. L. Dillamore and W. T. Roberts, Acta Metallurgica **12**, 281 (1964).

[93] T. Vecchione, D. Dowell, W. Wan, J. Feng, and H. Padmore, in *35th International Free-Electron Laser Conference* (New York, NY, 2013) pp. 424–426.

[94] N. D. Browning, (private comminication).

[95] D. Janssen, H. Büttig, P. Evtushenko, M. Freitag, F. Gabriel, B. Hartmann, U. Lehnert, P. Michel, K. Möller, T. Quast, B. Reppe, A. Schamlott, C. Schneider, R. Schurig, J. Teichert, S. Konstantinov, S. Kruchkov, A. Kudryavtsev, O. Myskin, V. Petrov, A. Tribendis, V. Volkov, W. Sandner, I. Will, A. Matheisen, W. Moeller, M. Pekeler, P. v. Stein, and C. Haberstroh, Nuclear Instruments and Methods in Physics Research Section A: Accelerators, Spectrometers, Detectors and Associated Equipment Proceedings of the 24th International Free Electron Laser Conference and the 9th Users Workshop., **507**, 314 (2003).

[96] J. Sekutowicz, J. Iversen, and G. Kreps, "Nb-Pb Superconducting RF-gun," TESLA-FEL 2005-09 (Deutsches Elektronen-Synchrotron (DESY), Hamburg, Germany, 2005).

[97] D. Laurent, C. Wang, and J. Callaway, Physical Review B **17**, 455 (1978).

[98] L. Mattheiss, Physical Review B **1**, 373 (1970).

[99] I. Petroff and C. Viswanathan, Physical Review B **4**, 799 (1971).

[100] H. Qian, C. Li, Y. Du, L. Yan, J. Hua, W. Huang, and C. Tang, Physical Review Special Topics - Accelerators and Beams **15**, 040102 (2012).

[101] J. K. Chen, D. Y. Tzou, and J. E. Beraun, International Journal of Heat and Mass Transfer **49**, 307 (2006).